Stress-Strain Behavior and Microstructural Evolution of Hot-Pressed Paper Webs Revealed by X-Ray Tomography

Amanda Mattsson [a,*] Arttu Miettinen [b] Tove Joelsson [c] Gunilla Pettersson [a] Per Engstrand [a] and Jukka A. Ketoja [a,d]

The mechanical performance of fiber-based materials depends not only on strength but also on elongation, which is particularly critical in converting and end-use applications. Wood-fiber-based materials, such as thermomechanical pulp (TMP) paper webs, are typically brittle and exhibit low breaking strain. However, both dry and wet strengths can be significantly improved through hot-pressing, especially in the presence of lignin. This study examines the influence of hot-pressing time on the complete stress–strain behavior of calendered TMP webs. Dry samples showed only minor, systematic changes in mechanical properties with increasing pressing time at 200 °C. In contrast, wet samples exhibited a pronounced increase in breaking strain for pressing times exceeding 1 s, accompanied by increased wet specific strength and tensile energy absorption. Wet stiffness also increased beyond what could be explained by densification alone, indicating enhanced inter-fiber bonding. To elucidate these effects, X-ray microtomography combined with image analysis was used to characterize microstructural features, including porosity, pore size, surface roughness, sheet thickness, and fiber wall density as functions of pressing time. The results demonstrate that extended hot-pressing promotes microstructural consolidation and bonding mechanisms that improve mechanical performance under both dry and wet conditions.

DOI: 10.15376/biores.21.2.3718-3732

Keywords: Hot-pressing; Mechanical properties; X-ray tomography; Microstructure; TMP; Lignin; Interdiffusion

Contact information: a: Department of Engineering, Mathematics and Science Education, Mid Sweden University, SE-85170 Sundsvall, Sweden; b: Department of Physics and Nanoscience Center, P.O. Box 35, FI-40014 University of Jyväskylä, Jyväskylä, Finland; c: RISE - Research Institutes of Sweden, Bioeconomy, Materials and Surfaces, 114 28 Stockholm, Sweden; d: VTT Technical Research Centre of Finland Ltd, P.O. Box 1000, FI-02044 Espoo, Finland;
** Corresponding author: amanda.mattsson@miun.se*

INTRODUCTION

Fibrous sheets, commonly manufactured through water-forming, foam-forming, or air-laid techniques, are materials composed of entangled fibers, forming a porous network. Typical examples include paper, cardboard, and a range of insulation materials. Among these, paper has been widely studied, especially regarding its stress–strain behavior, as strength is often its most critical performance parameter. The mechanical response of paper under tensile loading involves a complex interplay of viscoelastic, plastic, and inelastic deformation mechanisms, all governed by the evolving structure of the fiber network

(Coffin 2009). These properties are highly sensitive to moisture content, which modulates the molecular bonding mechanisms, primarily hydrogen bonding, between fibers and fibrils (Hirn and Schennach 2015). It is well known that moisture acts as a plasticizing agent for lignin by decreasing its glass transition temperature, thereby facilitating polymer mobility and interdiffusion at elevated temperatures (Back *et al.* 1983). Under elevated moisture conditions, hot-pressing can enhance bonding by promoting lignin interdiffusion at fiber interfaces, resulting in stronger and more ductile fiber–fiber connections even as hydrogen bonds are weakened (Joelsson 2021; Mattsson *et al*. 2021; Elf *et al*. 2025). Related behavior has recently been reported for binder-free, lignin-rich fiber networks produced using different forming methods, where hot-pressing resulted in pronounced increases in both dry and wet strength while retaining features of the original network structure (Paunonen *et al*. 2026). Comparable effects have been observed in other polymer systems, such as rubber, where extended hot-pressing increases elongation due to polymer interdiffusion (Gurney *et al.* 2017). Such improvements in ductility and strength are particularly desirable in applications such as sustainable packaging, where mouldability and toughness are key requirements.

Understanding how hot-pressing alters the mechanical properties of fibrous materials requires a simultaneous investigation of both their macroscopic stress–strain behavior and the microstructural transformations within the fiber network. The development of strength and ductility during hot-pressing is closely linked to changes in network characteristics such as fiber–fiber contact, bonding area, fiber orientation, and local density. However, traditional 2D imaging methods, such as optical or scanning electron microscopy, are insufficient for capturing true 3D architecture and its evolution during processing.

To address this limitation, X-ray microtomography offers a powerful method for visualizing and quantifying the internal structure of fiber networks in three dimensions by reconstructing a volumetric dataset from a stack of radiographic projections, from which internal cross-sections and three-dimensional renderings can be extracted. Recent advancements in laboratory and desktop-scale systems have made this technique more accessible, enabling *in situ* or *ex situ* imaging under various processing and loading conditions. When combined with image analysis, X-ray microtomography allows for the extraction of structural descriptors that can be directly correlated with mechanical performance.

In this study, X-ray microtomography was integrated with mechanical testing to investigate how hot-pressing time influences both the microstructure and the stress–strain response of fiber sheets. By linking structural evolution, such as changes in fiber bonding and network configuration to macroscopic mechanical behavior, the aim of this work was to identify the key mechanisms that govern strength and ductility in hot-pressed fiber materials. This unified approach provides a comprehensive framework for optimizing processing conditions and guiding the design of high-performance, bio-based materials.

EXPERIMENTAL

Hot-Pressing of Paper Sheets

Calendered industrial paper containing thermo-mechanical pulp (TMP) with a basis weight of 70 g/m² was used throughout this study. The sheets were hot-pressed using a planar hot-pressing system integrated into a servo-hydraulic testing machine (MTS

Systems, USA, 1980) and controlled by the MTS FlexTest60 hardware (2023) together with their software MPT (Multi-Purpose Testware). Heat was applied to the samples *via* heated plates positioned on both sides, ensuring uniform thermal transfer during pressing. Pressing times ranged from 0.05 to 30 seconds, with a constant applied pressure of 3.5 MPa and a temperature of 200 °C. This relatively low pressing temperature was selected to prevent degradation of cell wall polymers during longer pressing durations. All sheets were pressed in a dry state (7 ± 1 wt% moisture), ensuring consistent drying conditions and eliminating variables associated with different drying rates. Additionally, the use of calendered paper minimized density variations during hot-pressing, thereby allowing a clearer focus on the role of lignin interdiffusion in the analysis.

Physical Characterization

After hot-pressing, the sheets were conditioned according to ISO 187 (2022), followed by standard measurements of grammage, thickness, and density in accordance with ISO 536 (2019) and ISO 534 (2011). Mechanical parameters, including modulus, strength, and strain at break, were determined from the stress–strain curves. The modulus was calculated from the maximum slope of the curve, the strength was defined as the maximum stress reached, and the strain at break corresponded to the strain value at the point of maximum stress.

Tomographic Imaging

The sheets were imaged at the X-ray tomography laboratory of the University of Jyväskylä with two imaging resolutions, resulting in high-resolution views of smaller samples and large-area views of larger pieces of the sheet.

For high-resolution imaging, a 1.0 mm wide strip of the sheet was carefully cut with a surgical knife and glued to the tip of a carbon fiber rod with cyanoacrylate adhesive. The rod had a diameter of 1.0 mm, and the region to be imaged overhung the rod so that it was not affected by the glue. The rod was placed into the Xradia microXCT - 400 tomograph (Xradia Inc., Concord, CA, USA) and imaged with 40 kV acceleration voltage and 4 W X-ray tube power. A total of 1800 projections were acquired with 12 s exposure time each. The image pixel size was 0.58 µm (corresponding to 1.5 µm MTF10% spatial resolution) and the total imaging time (exposure + readout + movements) was approximately 10 h. The projection data was reconstructed using the Feldkamp-Davis-Kress formulation of cone-beam filtered back-projection algorithm (Feldkamp *et al*. 1984) implemented in the pi2 software into 3D volume images that show approximately 1 mm × 1 mm piece of the sheet (Fig. 1b). All microstructural images presented in this work represent two-dimensional cross-sections or three-dimensional renderings extracted from these reconstructed volumetric datasets, rather than surface images.

For large-area imaging, a similar sample preparation process was applied, but now an approximately 8 mm wide strip was glued into the tip of an acrylic rod of the same diameter. The imaging was performed with an in-house built JTomo cone-beam microtomograph. The X-ray source was set to 40 kV acceleration voltage and 4 W power. A total of 2940 projections were acquired, and the exposure time was 2 s per projection. The pixel size was 2.85 µm and the imaging time was 1.7 h. Reconstructions (Fig. 1a) were done similarly to the high-resolution case, but now the volume images show approximately 7 mm × 5 mm piece of the sheet, that is, 35 times larger area than the high-resolution images but with a 5-fold lower resolution.

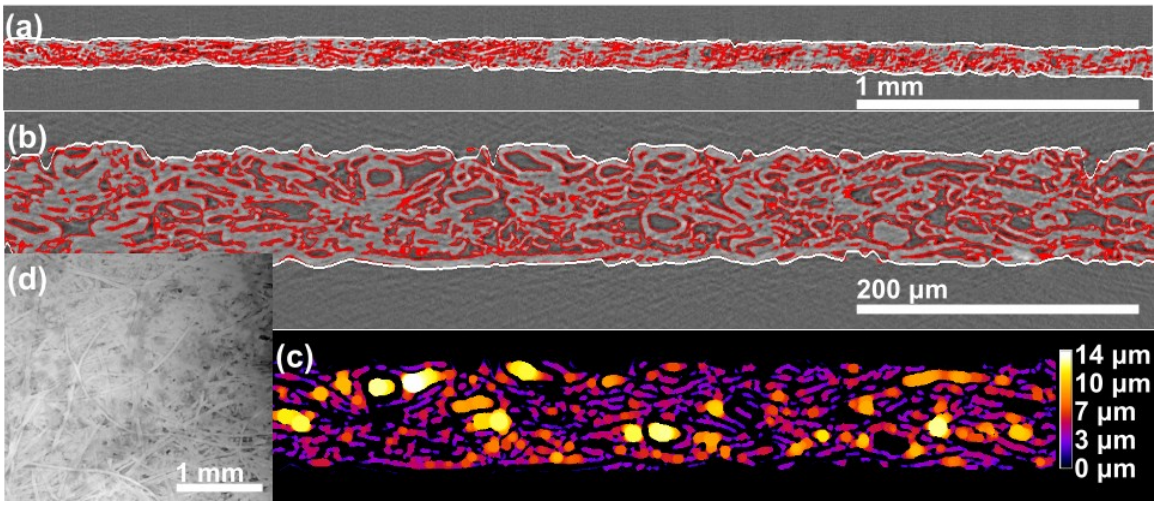

Fig. 1. Original tomographic cross-sections of a large area (low-resolution) (a) and a high-resolution image (b) overlaid with the top and bottom surface (white lines), and edges of segmented fibers (red lines around grey fiber cross-sections). The corresponding pore diameter map (c) shows local pore diameters with different colors, and the top surface height map (d) shows surface height variations as grey levels. The scale bars in (a) and (b) correspond to 1 mm and 200 µm, respectively. The scale bar in (d) corresponds to 1 mm. Panel (c) is on the same scale as (b).

Image analysis

The reconstructed 3D images were cropped and rotated manually such that any empty space around the sample was minimized, and the sample became as straight and horizontal as possible. The images were then denoised with the bilateral filter (Tomasi and Manduchi 1998) (spatial $\sigma = 2.5$ pixels, radiometric $\sigma = 0.0003$). The filtered images were segmented using the Otsu method (Otsu 1979) into binary images, where the air was denoted by pixels having the value zero, and fibers by pixels having the value one. The quality of the segmentation was controlled by visual checks (Figs. 1a and 1b).

To separate air space outside the sheet from pores, the surfaces of the sheet were found using the "Carpet" algorithm (Turpeinen *et al*. 2015), where a surface whose shape is governed by Edward-Wilkinson dynamics is fitted to the image data (surface tension = 1.0) (Figs. 1a and 1b). Effectively, the surface binds to the surface of the sheet despite it containing cavities and even holes in the case of very thin sheets. The method yields height maps of both surfaces of the sheet (Fig. 1d) that can, in turn, be used to calculate various surface roughness parameters for both surfaces and the true geometrical thickness of the sheet. Here, the root mean square (RMS) thickness calculated from height maps was used, where large wavelengths were removed using Gaussian high-pass filtering ($\sigma = 50$ µm) to avoid impacting the roughness values by the global (large-scale) curvature of the sample. Additionally, the surfaces effectively divide the air space into pores and air outside of the sample.

After the sheet surfaces have been found, it is trivial to calculate the porosity, ϕ, by counting air pixels between the surfaces, and the total number of pixels between the surfaces, and dividing these values. A pore diameter map can be calculated using the local thickness approach (Hildebrand and Ruegsegger 1997), where the pore diameter at a point in the pore space is defined as the diameter of the largest sphere that contains the point and fits entirely into the pore space (Fig. 1c). As defined, the pore diameter can be calculated for each pixel in the pore space using specific algorithms, and the diameter distribution of

pore volume is then easily found by statistical binning of all the diameter values in all the pore pixels. In principle, a similar process could be applied to the fiber phase, yielding fiber wall thickness distribution.

Microscopical quantities from imaging can be combined with more traditional laboratory measurements. For example, apparent sheet density ρ_{app} is usually determined from grammage G and apparent thickness d_{app} measured with a caliper thickness gauge as

$$\rho_{app} = \frac{G}{d_{app}} \quad (1)$$

As shown by Miettinen *et al*. (2015), the caliper thickness does not equal the true geometrical average thickness d of the sheet, if the surfaces of the sheet are rough. However, there are image-based or profilometry-based methods to convert between the caliper thickness and the true geometrical average thickness. By replacing the caliper thickness in Eq. 1 with the true geometrical thickness determined from volume image data, an estimate of the true sheet density ρ is attained as shown by Eq. 2:

$$\rho = \frac{G}{d} = \frac{GA}{V} \quad (2)$$

If the sheet does not contain fillers or other non-fiber solid phases, as is the case with the demonstration materials used here, the fiber wall density can be estimated as,

$$\rho_f = \frac{m_f}{V_f} = \frac{m}{V_f} = \frac{GA}{V_f} = \frac{GA}{V(1-\phi)} \quad (3)$$

where it is assumed that the mass of the entire sample m equals the mass of fibers m_f. The lateral area of the sample A, the total sheet volume V, the total fiber volume V_f, porosity ϕ and the thickness d are easy to determine from the image data and grammage G from laboratory measurements. It follows that Eqs. 2 and 3 are feasible in practice, too.

SEM Imaging

Morphological characterization was performed using a high-resolution scanning electron microscope (Tescan Maya3-2016, TESCAN Brno s.r.o., Brno, Czechia). The microscope operated at an accelerating voltage of 4.0 kV with a beam intensity of 1.0, using a working distance of approximately 7 mm.

Cross-sectional specimens were prepared by argon ion milling (IM4000Plus, Hitachi High-Tech Co., Tokyo, Japan). Prior to imaging, all samples were sputter-coated with a 5 nm thick layer of iridium to improve electrical conductivity.

RESULTS AND DISCUSSION

Structural Changes for Varied Hot-Pressing Time

Examples of high-resolution cross-sectional images obtained with X-ray microtomography for unpressed reference (Fig. 2a), 1 s of hot-pressing (Fig. 2b), and 30 s of hot-pressing (Fig. 2c) can be seen in Fig. 2. It is possible to observe densification, with a lower pore volume, from the reference (Fig. 2a) to the two hot-pressed sheets (Figs. 2b and 2c).

Porosity, average pore diameter, roughness, and sheet thickness for all cases are shown in Fig. 3. A total of 1 to 3 replicates of each sample and imaging mode were analyzed, and the error bars in Fig. 3 show the standard deviation over the replicates, where

available. Top and bottom root mean square (RMS) roughnesses $S_{q,top}$ and $S_{q,bottom}$ were combined into a single roughness value S_q with Eq. 4:

$$S_q = \sqrt{S_{q,top}^2 + S_{q,bottom}^2} \quad (4)$$

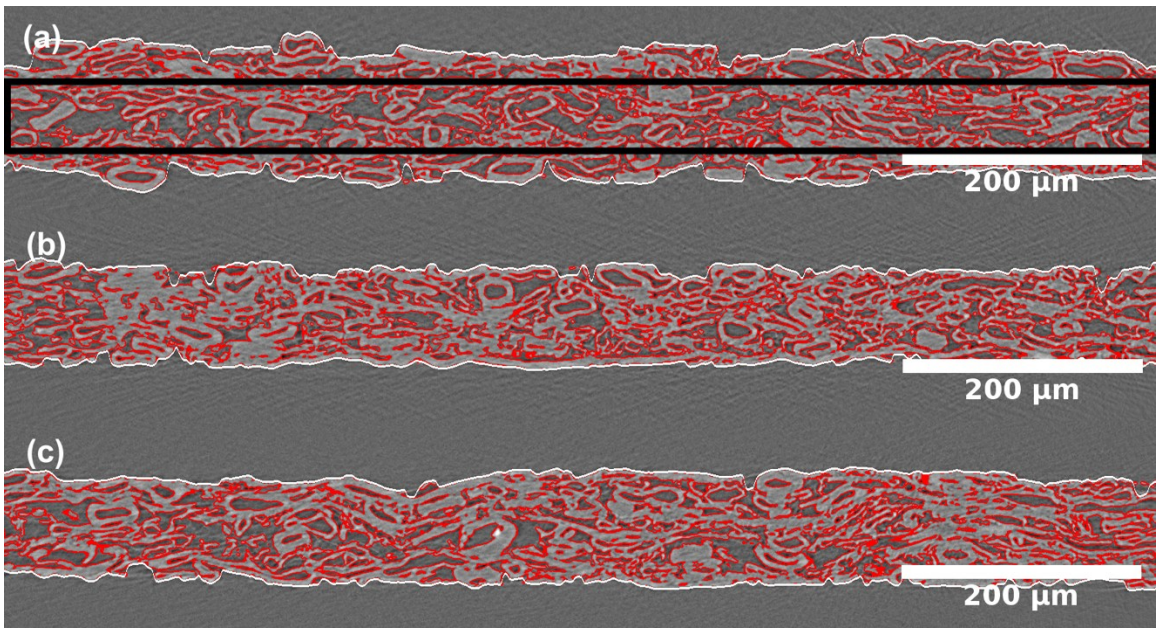

Fig. 2. Cross-sectional high-resolution X-ray microtomographic images of unpressed reference (a), 1 s hot-pressing (b), and 30 s hot-pressing (c). The black rectangle describes the region used for the calculation of the central porosity.

The porosity values in Fig. 3a are mostly below 0.5. In both high-resolution and large-area samples, porosity showed a decreasing trend with increasing pressing time, except for the 30 s pressing time point. In all cases, porosity values from the high-resolution images were larger than those calculated from the large-area images. This indicates that the materials contained pores that were not visible in the large-area images due to their limited spatial resolution. The same effect is shown also in the pore diameter values in Fig. 3b, where the average pore diameters calculated from the high-resolution images were approximately one-half of the values calculated from the large-area images, showing that the porosity not visible in the large-area images consisted of many rather small pores. As the difference between the two techniques increases as pressing time increased, it appears that the share of small pores not detectable in the large-area images increased with pressing time.

The behavior of the sheet roughness shown in Fig. 3c follows the porosity. In both high-resolution and large-area cases, the general trend was decreasing until the 30 s pressing time. In most cases, the high-resolution data showed smaller roughness values than the large-area data. The most probable reason for this behavior is that the large sheet areas contained grammage variation that is not visible in the high-resolution images. Such a variation is suggested by the large-area thickness (Fig. 3d), for which the changes with varied pressing time were similar.

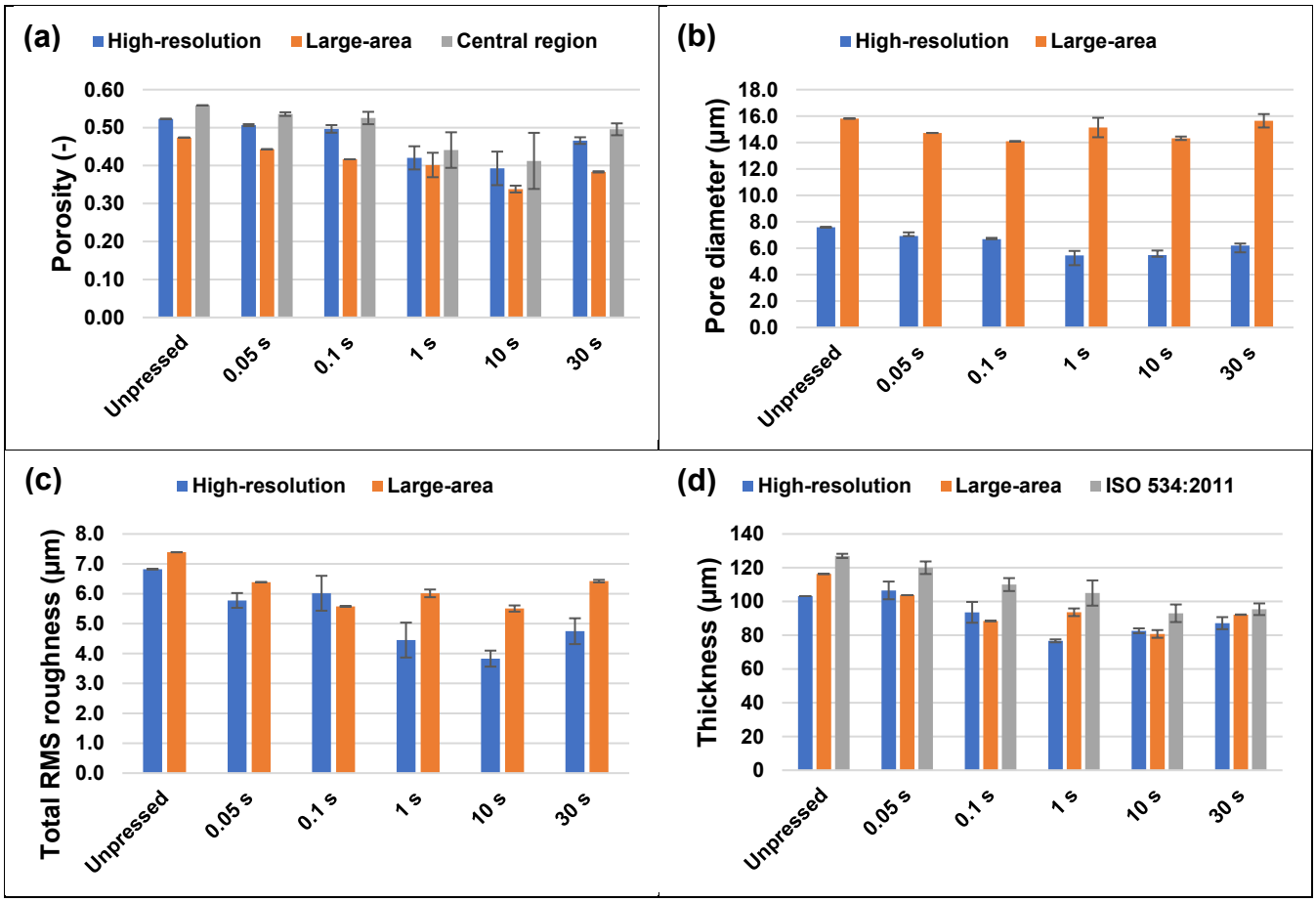

Fig. 3. Porosity (a), pore diameter (b), root mean square (RMS) roughness (c), and sheet thickness (d) measured from both high-resolution, large-area images, as well as the standard way of measuring thickness of paper (ISO 534:2011) and including the central porosity in figure (a). The bars are averages over n = 1 to 3 replicates, and the error bars are standard deviations of all the replicates.

To eliminate the influence of surface roughness, porosity was additionally measured in the central region of the samples, excluding both surfaces, using the high-resolution images. A rectangle in Fig. 2a schematically indicates the measured area, and the corresponding results are presented in Fig. 3a. Interestingly, the central region gives the highest porosity in all studied cases, even though the obtained values are quite close to those obtained from the high-resolution images with the surface porosity included. As this difference is seen also for the unpressed reference, the reason could be the densification of the surface caused by the wet pressing and calendaring operations during the web preparation. The sheet densities of samples subjected to different hot-pressing times are summarized in Table 1. The density values derived from X-ray microtomography were calculated from the grammage and the true geometrical sheet thickness using Eq. 2. As density is defined as grammage divided by sheet thickness, the sheet density (Table 1) and thickness (Fig. 3d) are directly interconnected through Eq. 2 and therefore exhibit inverse trends. As shown in Fig. 3d, the sheet thickness decreased with increasing hot-pressing time up to 1 s, after which it became saturated or slightly increased at longer pressing times. This behavior was reflected in the sheet density, which increased up to 1 s of pressing and showed no statistically significant changes for longer pressing times.

Table 1. Density (kg/m^3) of the Unpressed Reference Paper and Hot-Pressed Samples Obtained by Measuring the Thickness Using an X-Ray Tomography 3D Image and with a Standard Testing Method

Sheet Type	X-Ray Tomography		Standard (ISO 534: 2011)
	High-Resolution	Low-Resolution	
Reference	680	606	557 ± 2.3
0.05 s	660 ± 33	679	586 ± 6.4
0.1 s	753 ± 50	797	633 ± 6.0
1 s	916 ± 10	753 ± 18	668 ± 11
10 s	850 ± 15	875 ± 25	743 ± 7.0
30 s	806 ± 32	765 ± 1	727 ± 4.7

The hot-pressing time varied from 0.05 s to 30 s. Only one parallel sample was analyzed with X-ray tomography in the case of the reference and two shortest pressing times.

Thickness values derived from X-ray microtomography were systematically lower than those obtained using the standard method (ISO 534:2011), resulting in correspondingly higher density values. This difference is attributed to the influence of surface roughness in the standard method, which leads to an overestimation of thickness. The most pronounced increase in density occurred between the unpressed reference and the samples pressed for 0.1 s, corresponding to the time scale required to heat and soften the fibers during hot-pressing. The maximum density was reached at 1 s in the high-resolution tomographic measurements, while the low-resolution tomography and ISO measurements showed peak values at 10 s.

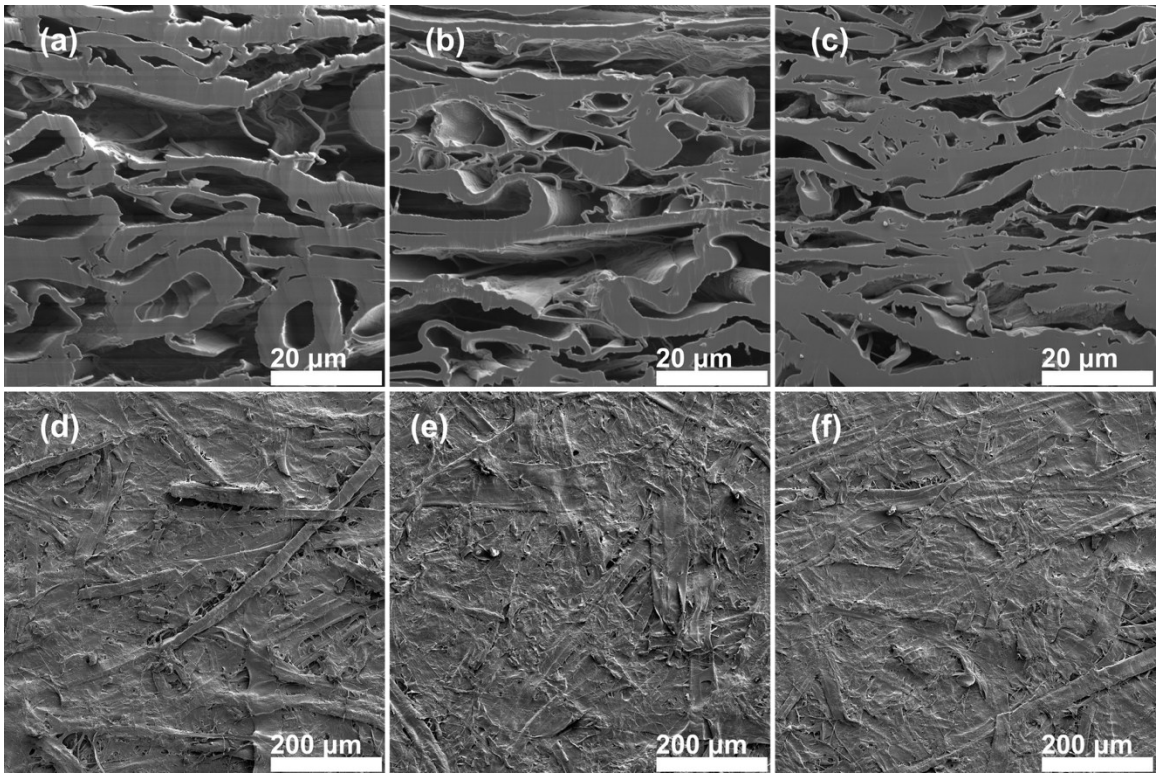

Fig. 4. Cross-sectional SEM images of unpressed reference (a), 1 s hot-pressing (b), and 30 s hot-pressing (c), and surface SEM images of unpressed reference (d), 1 s hot-pressing (e), and 30 s hot-pressing (f).

For longer pressing times, no further statistically significant densification was observed, suggesting that extended pressing induces structural changes beyond simple compaction.

Complementary insight into the morphological evolution during hot-pressing is provided by the corresponding SEM images shown in Fig. 4. The cross-sectional SEM micrographs (Figs. 4a–c) reveal the same trend observed in the X-ray microtomography: a progressive reduction in pore size and overall porosity from the unpressed reference to the samples hot-pressed for 1 s and 30 s. In the reference sheet, the fiber network remains loosely packed, whereas even short hot-pressing durations led to noticeable compaction and closer fiber–fiber contact. This initial densification can be attributed primarily to the preferential collapse of void space within the fiber network, as voids compress more readily than the solid cell wall material of the TMP fibers. After 30 s of pressing, the cross-section displays a markedly more consolidated structure with fewer and smaller voids. The surface SEM images (Figs. 4d–f) further confirm this densification. The initially rough and open surface of the reference sheet became increasingly smooth and uniform with pressing time, highlighting the collapse of surface pores and the improved inter-fiber bonding induced by hot-pressing.

As opposed to sheet density, fiber wall density in Fig. 5 also incorporates the porosity of the sheet, as shown in Eq. 3. The fiber wall density values determined from the high-resolution data show relatively small changes and no clear trend. The large-area fiber wall density data exhibits lower values and a minor increasing trend with increasing pressing time. This can be attributed to the fact that sub-pixel porosity, *e.g.*, submicron porosity or nanoporosity of the fiber wall, is not reflected in the porosity values measured from the large-area images due to spatial resolution constraints.

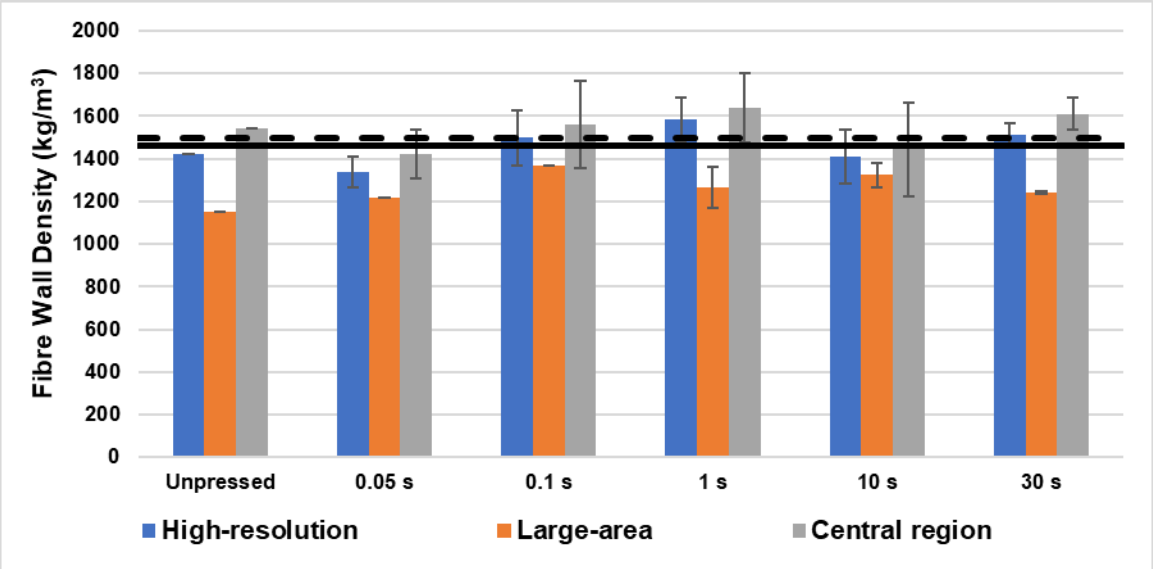

Fig. 5. Fiber wall density measured from grammage and image-based quantities. The solid line at 1460 kg/m^3 represents the average fiber wall density over all the high-resolution images, and the dashed line at 1500 kg/m^3 is the approximate earlier measured value for the density of wood fiber wall [Kellogg and Wangaard 1969]. The density of the crystal cellulose *Iβ* is 1610 kg/m^3 [Nishiyama *et al*. 2002].

The high-resolution data yielded averages of 1460 ± 90 kg/m^3 with surfaces included and 1535 ± 88 kg/m^3 when considering the sample central region only (see schematic image in Fig. 2a). These values are well comparable with the literature values, which range from 1440 kg/m^3 for amorphous cellulose to 1610 kg/m^3 for crystalline cellulose (Nishiyama *et al*. 2002; Sun 2005; Togawa and Kondo 2007; Ioelovich 2016). An approximate value of 1500 kg/m^3 for the density of wood fiber wall has been reported earlier (Kellogg and Wangaard 1969). Moreover, the level obtained here is close to the range 1440 to 1460 kg/m^3 reported earlier (Mattsson *et al*. 2021) using a similar image-based technique. However, the spread in the values obtained is rather large, perhaps due to the small region of each sample visible in the high-resolution images.

Stress-Strain Behavior

Figure 6 shows examples of stress-strain curves measured for both dry and wet samples. All dry samples behaved very similarly, with only minor changes in the specific modulus, breaking strain or specific strength (Fig. 7) obtained by dividing the stress and modulus by density. The specific modulus and strength are used throughout this article, which is equivalent to tensile modulus and tensile strength index commonly used in the pulp and paper community. As the relative bonded area is expected to be proportional to density, the specific modulus and strength effectively describe changes in the inter-fiber bonding properties. Interestingly, the specific modulus first dropped about 7% with 0.1 s pressing, but then it gradually increased according to lnt_p for longer pressing times t_p. However, the level remained below that of the reference up to 30 s pressing. Because of material densification, the elastic modulus increased from 6.4 GPa (reference) to 8.8 GPa (10 s pressing) when estimating sample thickness based on X-ray tomography.

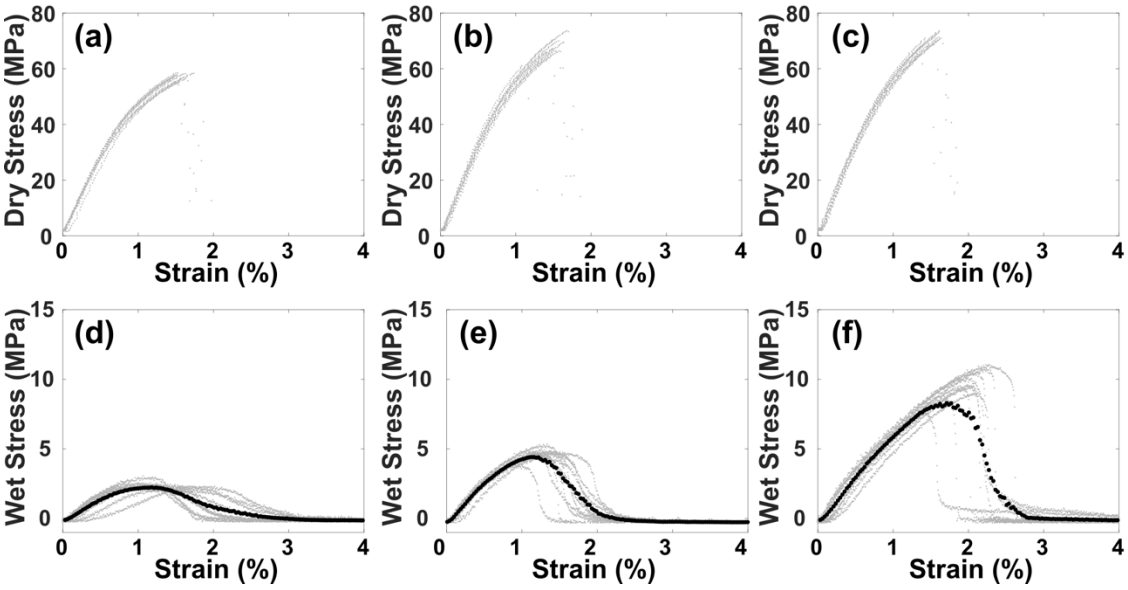

Fig. 6. Parallel stress-strain curves of both dry and wet hot-pressed samples. In the dry case, the behavior changes only very little between the reference paper (a) and the hot-pressed samples (b: 1 s and c: 30 s). In contrast, the changes in the stress-strain curves for the wet samples are rather large so that one moves from a rounded shape for the reference paper (d) to a shape that gradually resembles more and more a dry-strength curve when extending the pressing time (e: 1 s and f: 30 s). The parallel measurements (n = 10) are shown in grey, and additionally their average by the black curve for the wet stress curves.

As the breaking strain stayed very close to the reference value (Fig. 7b), the dry specific strength followed the same trend as the dry specific modulus (Figs. 7a and 7c) as there were no major changes in the shape of the stress-strain curve. The above drops in specific modulus and strength suggest that the new inter-fiber contacts formed with increased sample density did not bond properly at 200 °C when fibers were pressed dry.

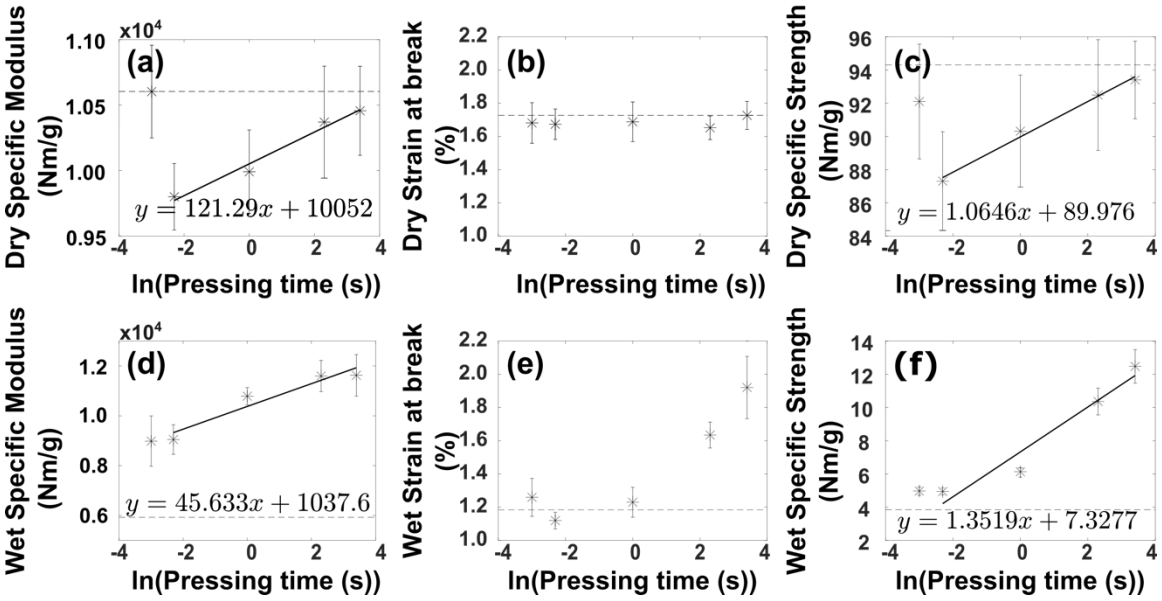

Fig. 7. Dry specific modulus (a), breaking strain (b), specific strength (c), and wet specific modulus (d), breaking strain (e), and specific strength (f) of the TMP paper, hot pressed at 200 °C with pressing times of 0.05 s, 0.1 s, 1 s, 10 s, and 30 s. The data were extracted from the corresponding stress-strain curves (Fig. 6). The dashed lines correspond to the values for the reference value, *i.e.* unpressed paper web. Data points represent mean values (n = 10), with error bars indicating 95% confidence intervals. The specific moduli and strengths fall on similar lines for pressing times exceeding 50 ms. The corresponding slopes (N·m·g^{-1}) are 121.3 (a), 1.1 (c), 45.6 (d), and 1.3 (f).

The behavior was quite different for the wet tensile properties. This is already apparent when looking at the stress-strain curves (Figs. 6d–f), whose shape changed from a rounded form for the reference paper to a steeper curve that began to resemble those of the dry samples when the pressing time became longer. A fracture in a wet hot-pressed sample did not happen as suddenly as in the case of dry samples, and there was a rather large scatter among parallel breaking strains. The measured specific modulus (Fig. 7d) was an order of magnitude smaller than for dry samples, and all measured stiffness values were higher than the value obtained for the wet reference paper. This is interesting especially in the case of the shortest pressing time of 0.05 s, for which the density and dry tensile properties did not change that much compared to the reference. Thus, even though fibers did not soften much with a very short pressure pulse, their surfaces still seemed to change so that wet bonding properties improved. The estimated elastic modulus increased from 0.42 GPa for reference to about 0.99 GPa for the 10 s pressed sheet.

Wet breaking strain (Fig. 7e) stayed rather close to the reference level up to 1 s pressing but then began to increase significantly with the longer pressing times of 10 and 30 s. This led to similar developments in the wet specific strength (Fig. 7f), which increased according to lnt_p beyond t_p = 1 s, as found earlier for the dry samples beyond t_p = 0.11 s. Based on earlier experiments and molecular simulations on lignin interdiffusion (Elf *et al.*

2025), these trends would be expected to continue if longer pressing times were applied. Moreover, the effects could be even stronger if the pressing temperature was increased. In addition, the wet breaking strain achieved the level of the dry one for the longest pressing time. Despite the above different levels of dry and wet strength, they both increased with almost equal slope for longer pressing time (Fig. 7). This suggests that the strength improvement in both cases originated from new inter-fiber bonds (or bonded area), which were equally strong in dry and wet conditions. Thus, the associated molecular bonding mechanism has to differ from hydrogen bonds of the reference web and is rather related to lignin interdiffusion that acted similarly for both the dry and wet cases. A similar result was obtained by Paunonen *et al*. (2026) when comparing dry and wet strength for different forming methods, where the two data sets overlapped after shifting the wet strength values by a level corresponding to the dry strength prior to hot pressing.

In the future, it will be interesting to study the increased elongation for even longer hot-pressing times and investigate whether it can improve material mouldability in applications. Another interesting topic would be applying micromechanical models (Orgéas *et al.* 2021; Miled *et al.* 2011) to estimate the thickness of lignin interfaces at joint regions that would reproduce the experimental findings. In this way, a fundamental understanding of parallel strengthening mechanisms on different scales could be achieved.

Future Work

While the present study demonstrated clear correlations between hot-pressing conditions, three-dimensional microstructural evolution, and macroscopic mechanical performance, the molecular-level mechanisms underlying the observed improvements in strength and ductility remain to be fully resolved. In particular, further work is needed to disentangle the relative contributions of lignin polymeric flow, interdiffusion, and intermixing under wet hot-pressing conditions from potential increases in other molecular bonding mechanisms within the cellulosic and holocellulosic components of the fiber network. Future studies combining X-ray microtomography with surface-sensitive chemical analysis techniques, such as X-ray photoelectron spectroscopy or spectroscopic mapping, together with multiscale molecular modeling, could provide direct insight into the evolution of interfacial chemistry and bonding during pressing and enable a more quantitative linkage between interfacial interactions, network structure, and the mechanical properties of hot-pressed fiber-based materials. In addition, future work could explore *in situ* optical microscopy of the sheet edge during hot pressing by positioning the sample near the press plate edge, thereby enabling time-resolved observations of structural evolution in the fiber network and complementing tomographic and chemical analyses.

CONCLUSIONS

1. Three-dimensional imaging methods were shown to be effective for obtaining detailed and reliable information on the microstructure of fibrous sheet materials. The high-resolution images enabled accurate quantification of porosity, pore size, and fiber wall density as functions of hot-pressing time.
2. Hot-pressing had a pronounced effect on the stress–strain behavior of wet samples, while only minor but systematic changes were observed in the dry mechanical properties. Fracture in wet hot-pressed samples occurred more gradually than in dry

samples, and a relatively large scatter in breaking strain was observed among parallel measurements. With increasing pressing time, the wet stress–strain curves evolved from a rounded shape characteristic of the reference paper to steeper curves that increasingly resembled those of the dry samples.

3. The wet breaking strain increased significantly for pressing times exceeding 1 s. Together with the concurrent increase in wet specific strength, this resulted in substantially higher tensile energy absorption compared with the reference paper.
4. The similar trends observed in dry and wet mechanical properties as a function of pressing time indicate that strength enhancement is likely governed by comparable molecular bonding mechanisms in both cases.

ACKNOWLEDGMENTS

The authors would like to acknowledge the ERD Fund (grant 20361245), the ÅForsk Foundation (grants 21-376 and 21-369), and the Neopulp research profile financed by the Knowledge Foundation for their support. J.A.K. is grateful for the support from Research Council of Finland (Grant No. 362363, Project "Forming and advanced characterization of monomaterial lignocellulosic packaging structure"). X-ray tomography experiments leading to this publication were performed in the X-ray Tomography laboratory of the University of Jyväskylä, Finland.

Conflict of Interest

The authors declare no conflict of interest.

Use of Generative AI

Generative artificial intelligence (ChatGPT, OpenAI) was used solely to improve the grammar and clarity of the manuscript text. The tool was not used for data analysis or for the preparation of images, figures, graphs, or diagrams. The authors are fully responsible for the content.

REFERENCES CITED

Back, E. L., Salmén, L., and Richardson, G. (1983). "Transient effects of moisture sorption on strength properties of paper and wood-based materials," *Svensk Papperstidning* 86(6), R61-71.

Coffin, D. W. (2009). "Developing a deeper understanding of the constitutive behavior of paper" in: *Advances in Pulp and Paper Research, Oxford 2009, Trans. of the XIVth Fund. Res. Symp. Oxford, 2009*, S. J. I'Anson, (ed.), pp 841-875, FRC, Manchester, 2018. https://doi.org/10.15376/frc.2009.2.841

Elf, P., Mattsson, A, Paajanen, A, Ketoja, J. A., Pettersson, G., Sanchez-Salvador, J. L., Blanco, A., Negro, C., Engstrand, P., Hedenqvist, M. S., and Nilsson, F. (2025). "Role of lignin in hot-pressing of paper: Insights from molecular simulations and experiments," *Biomacromolecules* 26(9), 5965-5978. https://doi.org/10.1021/acs.biomac.5c00872

Feldkamp, L. A., Davis, L. C. and Kress, J. W. (1984). "Practical Cone-Beam algorithm," *Journal of the Optical Society of America A* 1, 612-619. https://doi.org/10.1364/JOSAA.1.000612

Gurney, R., Henry, A., Schach, R., Lindner, A., and Creton, C. (2017). "Molecular weight dependence of interdiffusion and adhesion of polymers at short contact times," *Langmuir* 33, 1670-1678. https://doi.org/10.1021/acs.langmuir.6b03972

Hildebrand, T., and Ruegsegger, P. (1997). "A new meth-od for the model-independent assessment of thickness in three-dimensional images," *Journal of Microscopy* 185(1), 67-75. https://doi.org/10.1046/j.1365-2818.1997.1340694.x

Hirn, U., and Schennach, R. (2015). "Comprehensive analysis of individual pulp fiber bonds quantifies the mechanisms of fiber bonding in paper," *Sci. Rep.* 5(1), article 10503. https://doi.org/10.1038/srep10503

Ioelovich, M. Ya. (2016). "Models of supramolecular structure and properties of cellulose," *Polymer Science Series A* 58, 925-943. https://doi.org/10.1134/S0965545X16060109

ISO 534 (2011). "Paper and board — Determination of thickness, density and specific volume," International Organization for Standardization, Geneva, Switzerland.

ISO 536 (2019). "Paper and board — Determination of grammage," International Organization for Standardization, Geneva, Switzerland.

ISO 187 (2022). "Paper, board and pulps — Standard atmosphere for conditioning and testing and procedure for monitoring the atmosphere and conditioning of samples," International Organization for Standardization, Geneva, Switzerland.

Joelsson, T. (2021). *The Influence of Pulp Type and Hot-Pressing Conditions on Paper Strength Development*, PhD thesis, Mid Sweden University, Sundsvall, Sweden.

Kellogg, R. M., and Wangaard, F. F. (1969). "Variation in the cell-wall density of wood," *Wood Fiber Science* 3, 180-203.

Mattsson, A., Joelsson, T., Miettinen, A., Ketoja, J. A., Pettersson, G., and Engstrand, P. (2021). "Lignin inter-diffusion underlying improved mechanical performance of hot-pressed paper webs," *Polymers* 13(15), article 2485. https://doi.org/10.3390/polym13152485

Miettinen, A., Ekman, A., Chinga Carrasco G., and Kataja, M. (2015). "Measuring intrinsic thickness of rough membranes: application to nanofibrillated cellulose films," *Journal of Materials Science* 50, 6926-6934. https://doi.org/10.1007/s10853-015-9243-2

Miled, K., Sab, K., and Le Roy, R. (2011). "Effective elastic properties of porous materials: Homogenization schemes vs. experimental data," *Mechanics Research Communications* 38(2), 131-135. https://doi.org/10.1016/j.mechrescom.2011.01.009

Nishiyama, Y., Langan, P., and Chanzy, H. (2002). "Crystal structure and hydrogen-bonding system in cellulose Iβ from synchrotron X-ray and neutron fiber diffraction," *Journal of American Chemical Society* 124(13), 9074-9082. https://doi.org/10.1021/ja0257319

Orgéas, L., Dumont, P. J. J., Martoïa, F., Marulier, C., Le Corre, S., and Caillerie, D. (2021). "On the role of fiber bonds on the elasticity of low-density papers: A micro-mechanical approach," *Cellulose* 28, 9919-9941. https://doi.org/10.1007/s10570-021-04098-w

Otsu, N. (1979). "A threshold selection method from gray-level histograms," *IEEE Transactions on System, Man, and Cybernetics* 9(1), 62-66. https://doi.org/10.1109/TSMC.1979.4310076

Paunonen, S., Mattsson, A., Pettersson, G., and Ketoja, J. A. (2026). "Property variations of binder-free lignin-rich fiber networks driven by forming processes and hot pressing," *ACS Omega* 11(5), article 5c06266. https://doi.org/10.1021/acsomega.5c06266

Sun, C. (2005). "True density of microcrystalline cellulose," *Journal of Pharmaceutical Sciences* 94(10), 2132-2134. https://doi.org/10.1002/jps.20459

Togawa, E., and Kondo, T. (2007). "Unique structural characteristics of nematic ordered cellulose—Stability in water and its facile transformation," *Journal of Polymer Science* 45, 2850-2859. https://doi.org/10.1002/polb.21297

Tomasi, C. and Manduchi, R. (1998). "Bilateral filtering for gray and color images," in: *Sixth International Conference on Computer Vision*, Bombay, India.

Turpeinen, T., Myllys, M., Kekäläinen, P., and Timonen, J. (2015). "Interface detection using a quenched-noise version of the Edwards–Wilkinson equation," *IEEE Transactions on Image Processing* 24(12), 5696-5705. https://doi.org/10.1109/TIP.2015.2484061

Article submitted: January 2, 2026; Peer review completed: January 31, 2026; Revised version received: February 6, 2026; Accepted: February 17, 2026; Published: March 3, 2026.
DOI: 10.15376/biores.21.2.3718-3732